Ultrafast optical ranging
using microresonator soliton frequency combs

P. Trocha,[1*] M. Karpov,[2*] D. Ganin,[1*] M. H. P. Pfeiffer,[2] A. Kordts,[2] S. Wolf,[1]
J. Krockenberger,[1] P. Marin-Palomo,[1] C. Weimann,[1,4] S. Randel,[1,3] W. Freude,[1,3]
T. J. Kippenberg,[2,†] C. Koos[1,3,‡]

[1]Institute of Photonics and Quantum Electronics (IPQ),
Karlsruhe Institute of Technology (KIT), 76131 Karlsruhe, Germany
[2]Laboratory of Photonics and Quantum Measurements (LPQM),
École Polytechnique Fédérale de Lausanne (EPFL), CH-1015 Lausanne, Switzerland
[3]Institute of Microstructure Technology (IMT),
Karlsruhe Institute of Technology (KIT), 76131 Karlsruhe, Germany
[4]Now with: Corporate Research and Technology, Carl Zeiss AG, Oberkochen, Germany
[*] These authors contributed equally to the work
[†] E-mail: tobias.kippenberg@epfl.ch
[‡] E-mail: christian.koos@kit.edu.

Light detection and ranging is widely used in science and industry. Over the last decade, optical frequency combs were shown to offer unique advantages in optical ranging, enabling fast distance acquisition with high accuracy. Driven by emerging high-volume applications such as industrial sensing, drone navigation or autonomous driving, there is now a growing demand for compact ranging systems. Here we show that soliton Kerr comb generation in integrated microresonators provides a route to high-performance chip-scale ranging systems. We demonstrate dual-comb distance measurements with Allan deviations down to 12 nm at averaging times of 13 μs along with ultra-fast

1

ranging at acquisition rates of 100 MHz, allowing for in-flight sampling of gun projectiles moving at 150 m/s. Combining integrated soliton-comb ranging systems with chip-scale nanophotonic phased arrays could enable compact ultra-fast ranging systems for emerging mass applications.

Laser-based light detection and ranging (LIDAR) is a key technology in industrial and scientific metrology, offering high precision, long range, and fast acquisition (*1, 2*). LIDAR systems have found their way into a wide variety of applications, comprising, e.g., industrial process monitoring, autonomous driving, satellite formation flying, or drone navigation. When it comes to fast and accurate ranging over extended distances, optical frequency combs (*3*) have been demonstrated to exhibit unique advantages, exploiting time-of-flight (TOF) schemes (*4*), interferometric approaches (*5*), or combinations thereof (*6*). In early experiments (*4*), mode-locked fiber lasers were used for TOF ranging, thereby primarily exploiting the stability of the repetition rate. Regarding interferometric schemes, optical frequency combs were exploited to stabilize the frequency interval between continuous-wave (CW) lasers used in synthetic-wavelength interferometry (*5, 7*). Dual-comb schemes, which rely on multi-heterodyne detection by coherent superposition of a pair of slightly detuned frequency combs (*8*), allow to combine TOF measurements with optical interferometry, thereby simultaneously exploiting the radio-frequency coherence of the pulse train and the optical coherence of the individual comb tones (*6*). More recently, comb-based schemes have been demonstrated as a viable path to high-speed sampling with acquisition times down to 500 ns (*9*).

However, besides accuracy and acquisition speed, footprint is becoming increasingly important for LIDAR systems. On the technology side, recent advances in photonic integration show that large-scale nanophotonic phased arrays (*10, 11*) open a promising path towards ultra-compact systems for rapid high-resolution beam steering. To harness the full potential of these approaches, the optical phased arrays need to be complemented by chip-scale LIDAR engines

that combine high precision with ultrafast acquisition and that are amenable to chip-scale integration. Existing dual-comb LIDAR concepts cannot fulfill these requirements since they either rely on cavity-stabilized mode-locked fiber lasers (*6*) or on spectral broadening of initially narrowband seed combs (*9*), which typically require delicate fiber-based dispersion management schemes, usually in combination with intermediate amplifiers.

Here we show that microresonator-based dissipative Kerr-soliton (*12,13*) (DKS) comb sources provide a route to integrated LIDAR systems that combine sub-wavelength accuracy and unprecedented acquisition speed with scalable fabrication, robust implementation and compact form factors. DKS are solutions of a driven, damped and detuned Nonlinear Schrödinger equation, often referred to as Lugiato-Lefever equation (*14*). Such ultra-short temporal solitons can circulate continuously in the cavity, relying on a double balance of dispersion and nonlinearity as well as parametric gain and cavity loss (*13*). In the frequency domain, DKS pulse trains correspond to optical frequency combs, which combine large bandwidths and smooth spectral envelopes with free spectral ranges in the range from tens of gigahertz to a few terahertz. Microresonator-based DKS have recently been used in dual-comb spectroscopy (*15*), coherent communications (*16*), and frequency metrology (*17*). In our demonstrations, we exploit DKS combs for synthetic-wavelength interferometry with massively parallel multi-heterodyne detection. Our scheme is based on a pair of free-running comb generators and does not require phase-locking of the combs to each other. The large optical bandwidth of more than 11 THz leads to highly precise distance measurements with Allan deviations reaching 12 nm at an averaging time of 14 μs, while the large FSR enables high-speed measurements at rates of up to 100 MHz. We prove the viability of our technique by sampling the naturally scattering surface of air-gun projectiles on the fly, achieving lateral spatial resolutions of better than 2 μm for object speeds of more than 150 m/s.

For DKS comb generation, we use a pair of CW-pumped silicon nitride microring resonators

3

on separate chips. The devices (Fig. 1A) are fabricated using the photonic Damascene process (*18*), enabling waveguide cross sections of $1.65\,\mu$m$\times 0.8\,\mu$m. DKS comb generation is achieved by sweeping the pump laser frequency from the effectively blue-detuned to a defined point in the effectively red-detuned regime of a selected cavity resonance, where the microresonator system supports soliton formation (*19*) (Fig. 1B). Once the laser scan stops, typically a multi-soliton state is generated. By next applying the backward frequency tuning technique (*19*), a single-soliton state corresponding to an optical frequency comb with spectrally smooth sech^2-shape envelope (Fig. 1C) is achieved in a deterministic manner. A more detailed description of the experimental setup and of the microresonator devices can be found in (*20*).

The experimental setup used for dual-comb ranging is depicted in Fig. 2A. For multi-heterodyne detection, we use two Kerr comb generators with slightly different free spectral ranges of $\omega_{\mathrm{S,r}}/2\pi = 95.842\,\mathrm{GHz}$ and $\omega_{\mathrm{LO,r}}/2\pi = 95.746\,\mathrm{GHz}$ respectively. To demonstrate that our concept does not require phase locking of the DKS combs, we used a pair of free-running continuous-wave (CW) lasers to pump the microresonators and compensate for the stochastic phase drifts by digital signal processing (DSP) (*20*). The pump light for the signal and the LO comb is amplified by erbium-doped fiber amplifiers (EDFA) to power levels of 3.5 W and 2.6 W, respectively, and then coupled to the microresonator chips with a coupling efficiency of approximately 60 % per facet. The resulting combs feature overall power levels of 4.3 mW and 2.5 mW and are amplified by a pair of C+L band EDFA to 450 mW to improve the measurement accuracy. The spectra of the amplified combs are shown in Fig. 2C . The gain bandwidth of the EDFA limits the number of usable lines to about 115, which is sufficient for our experiments.

For distance measurements, the signal comb is split by a fiber-based 50:50 coupler, and one part is routed to the target and back to a balanced measurement photodetector (meas. PD), while the other part is directly sent to the balanced reference detector (ref. PD), see Fig. 2A. Measurement and reference PD feature bandwidths of 43 GHz. Similarly, the LO comb is

4

split in two portions, which are routed to the measurement PD and the reference PD for multi-heterodyne detection. The resulting baseband signal contains discrete beat notes, which are recorded by a 33 GHz real-time sampling oscilloscope and separated by means of a numerically calculated Fourier transformation. The distance to the target is extracted from the phase of the baseband beat notes. Data processing and evaluation is performed offline, see (20) for details of the underlying algorithms.

Figure 2B shows the Fourier transform of a recorded baseband signal, revealing the various beat notes between the signal and LO comb lines. The spacing of the beat notes is given by the difference of the line spacing of the LO and the signal comb and amounts to $\Delta f_{\mathrm{r}} = \Delta \omega_{\mathrm{r}}/2\pi =$ 96.4 MHz, thereby dictating a minimum possible acquisition time of $T_{\mathrm{min}} = 1/\Delta f_{\mathrm{r}} = 10.4$ ns and a maximum possible distance acquisition rate of 96.4 MHz.

For a thorough stability and precision analysis of our dual-comb scheme, we measure the distance to a static mirror and evaluate the Allan deviation. The entire measurement contains a series of $\approx 1.1 \cdot 10^6$ individual data points taken at an acquisition time of 10.4 ns per point, leading to a total duration of ≈ 12 ms. The extracted Allan deviation is plotted in Fig. 2D. At an averaging time of 10.4 ns, the Allan deviation amounts to 284 nm, and it decreases to 12 nm for an averaging time of 13 μs. At small averaging times, the Allan deviation decreases with increasing averaging time, as expected for dominating white noise such as shot noise or amplified spontaneous emission (ASE) originating from the EDFA. For larger averaging times, the Allan deviation increases, which we attribute to thermal drift of the fibers and to mechanical vibrations at acoustic frequencies. The current measurement accuracy is hence only limited by a non-ideal implementation of the system. Further improvements are possible by reducing the ASE noise floor of the EDFA and by avoiding thermal drift and mechanical vibrations. Fundamentally, the measurement accuracy is only limited by inevitable shot noise and possibly by additional ASE noise of ideal EDFA. For comb powers of 10 mW, this would allow for

measurement accuracies of better than 10 nm at the highest acquisition rate of 100 MHz, see (*20*) for details.

Besides the Allan deviation, we also estimated the accuracy of our technique by measuring variable distances to a target that is moved over a full ambiguity distance $L_{amb} = \frac{c}{2}\frac{2\pi}{\omega_{r,S}}$ (Fig. 2E). In this experiment, the target mirror is stepped in increments of $50\,\mu$m using a feedback-stabilized stage with a positioning accuracy of better than 50 nm. To reduce the impact of fiber drift, the distance measurement is continuously switched between the movable target mirror and a static calibration mirror in quick succession, taking between 6 500 and 9 500 measurements with the full acquisition rate of approximately 96 MHz on each mirror, see (*20*). From these measurements, we extract the distance to the target mirror and the associated standard deviation, see (*20*) for details. In the upper part of Fig. 2E, the measured distance is plotted as a function of the distance set by the translation state. Measured distances exceeding the ambiguity distance of $L_{amb} = 1.56$ mm are unwrapped manually. The bottom part of Fig. 2E shows the residual deviations of the measured positions from the set positions along with the respective standard deviations indicated as error bars. Importantly, no cyclic error is observed throughout the ambiguity distance. We determine the accuracy of our measurement to 188 nm, defined as the standard deviation of the residuals, which are of the same order of magnitude as the 50 nm positioning accuracy of the stage specified by the manufacturer. In this measurement, the refractive index of air is considered according to Ciddors formula for ambient lab conditions. Note that the measured 188 nm standard deviation of the residuals is still dominated by drift and acoustic vibrations of the measurement setup rather than by the measurement system itself, despite compensation via the static calibration mirror. This can be inferred from the fact that the standard deviation of 188 nm is still much larger than the intrinsic system-related errors of 5 nm that should be expected for the averaging time of $100\,\mu$s, see (*20*) for a more detailed discussion.

To validate the reproducibility of our system and to benchmark the results with respect to existing techniques, we measure the profile of a quickly rotating disk having grooves of different depths on its surface, see Fig. 3A. In this experiment, the measurement beam is focused to the surface near the edge of the disk which rotates at a frequency of about 600 Hz thus resulting in an edge velocity of 160 m/s. The distance acquisition rate in this experiment amounts to 96.5 MHz, limited by the spectral spacing of $\Delta\omega_\mathrm{r}/2\pi$ of the beat notes in the baseband photocurrent, but not by the acquisition speed of our oscilloscopes. The resulting profiles are shown in Fig. 3B for two measurements, which were taken independently from one another during different round trips of the disc. Measurement points close to the edges of the grooves may suffer from strong scattering and low power levels, which lead to unreliable distance information. Using the fit error of the linear phase characteristic as a quality criterion, our technique allows to identify such non-usable measurement points and to automatically discard them from the data, see (20) for details. The raw data of both measurements was further subject to vibrations of the disk arising from the driving engine. These vibrations have been removed by fitting a polynomial to the top surface of the disk and by using it for correction of the overall measurement data. In a first experiment, we analyze the reproducibility of the technique by a detailed comparison of the results obtained from the two measurements, see Fig. 3B, Inset 1. The measured profiles exhibit good agreement regarding both macroscopic features such as the groove depth as well as microscopic features such as surface texture and a decrease of depth towards the edge of the groove. Deviations are attributed to the fact that the two measurements have been taken independently and might hence not have sampled the exactly same line across the groove. In addition, we benchmark our technique by comparing the obtained profile of a single groove with a profile obtained from an industrial optical coordinate measuring machine (CMM, Werth VideoCheck HA), Fig. 3B, Inset 2. Both profiles are in good agreement, with some minor deviations that we again attribute to slightly different measurement positions along the analyzed groove.

Ultrafast ranging is demonstrated by measuring the profile of a flying air-gun bullet that is shot through the focus of the measurement beam, see Fig. 3C. The projectile moves at a speed of 150 m/s (Mach 0.47), which, together with the acquisition rate of 96.2 MHz, results in a lateral distance of 1.6 μm between neighbouring sampling points on the surface of the bullet. The full profile of the projectile is taken during a single shot and depicted in red in Fig. 3D along with a reference measurement obtained from the static bullet using a swept-source optical coherence tomography system (dark blue). For better comparison, the two profiles were rotated and an actual speed of the bullet of 149 m/s was estimated for best agreement. Both curves clearly coincide and reproduce the shape of the fired projectile. Missing data points in the dual-DKS-comb measurement at the tip of the projectile are caused by low power levels of the back-coupled signal, which is inevitable for such steep surfaces in combination with the limited numerical aperture of the lens used for collecting the backscattered light. As before, these measurement points have been discarded from the data based on a large fit error of the linear phase characteristic (*20*). An image of the projectile after recovery from the backstop exhibits a strong corrugation of the bullet towards its back, Fig. 3E. This leads to deviations of the measured profiles in Fig. 3D towards the right-hand side, since the strongly corrugated surface of the projectile in this area has very likely been sampled at two different positions.

To make dual DKS-comb ranging a viable option for practical applications, the limited ambiguity distance of 1.56 mm must be overcome. This can, e.g., be achieved by switching the role of the LO comb and the measurement comb (*6*) or by sending the LO comb also to the target while evaluating not only the difference signal of the balanced photodetectors, but also the sum, see (*21*). Using such techniques, high-precision ranging over extended distances should be possible, only limited by coherence lengths of the individual comb lines, which amount to several kilometers. Note that the high acquisition rate allows to track continuous movements of objects at any practical speed, with an ambiguity limit of $\approx 145\,000$ m/s.

Our experiments demonstrate the viability of chip-scale DKS comb generators to act as optical sources for high-performance ranging systems and are a key step towards fully integrated chip-scale LIDAR engines, as illustrated as an artist's view in Fig. 4. In this vision, the LIDAR system is realized as a photonic multi-chip assembly, in which all photonic integrated circuits are connected by photonic wire bonds, Inset (2) (*22*). The comb generators are pumped by integrated continuous-wave lasers, and a dedicated optical chip is used to transmit and receive the optical signals. The receiver is equipped with a chip-attached micro-lens that collimates the emitted light towards the target, Inset (3) (*23*). The electrical signals generated by the photodetectors are sampled by analog-to-digital converters (ADC) and further evaluated by digital signal processing in powerful field-programmable gate arrays (FPGA) or application-specific integrated circuits (ASIC). Note that free-running pump lasers greatly simplify the implementation in comparison to configurations where two comb generators are simultaneously pumped by a single light source. While most of the technological building blocks for realizing this vision have already been demonstrated, one of the remaining key challenges is to reduce the power levels required for DKS generation to typical output power levels of state-of-the-art diode lasers. This requires silicon nitride microresonators with higher quality factors which can be achieved by optimizing the waveguide geometry and the fabrication processes. We expect that such optimizations will allow to increase the Q-factor by about one order of magnitude, thus reducing the pump power requirements by two orders of magnitude. Alternatively, other integration platforms such as silicon oxide or AlGaAs can be used, permitting comb generation with only a few milliwatts of pump power (*24*). These power levels are realistically achievable with integrated pump laser diodes. Based on these findings, we believe that DKS-based dual-comb LIDAR could have transformative impact on all major application fields that require compact LIDAR systems and high-precision ranging, in particular when combined with large-scale nanophotonic phased arrays (*10, 11*). Acquisition rates of hundreds of megahertz could enable ultrafast

3D imaging with megapixel resolution and update rates of hundreds of frames per second.

References

1. M.-C. Amann, T. Bosch, M. Lescure, R. Myllyla, M. Rioux, *Optical Engineering* **40**, 10 (2001).

2. G. Berkovic, E. Shafir, *Advances in Optics and Photonics* **4**, 441 (2012).

3. T. Udem, R. Holzwarth, T. W. Hänsch, *Nature* **416**, 233 (2002).

4. K. Minoshima, H. Matsumoto, *Applied Optics* **39**, 5512 (2000).

5. N. Schuhler, Y. Salvadé, S. Lévêque, R. Dändliker, R. Holzwarth, *Optics Letters* **31**, 3101 (2006).

6. I. Coddington, W. C. Swann, L. Nenadovic, N. R. Newbury, *Nature Photonics* **3**, 351 (2009).

7. Y.-S. Jang, *et al.*, *Scientific Reports* **6**, srep31770 (2016).

8. F. Keilmann, C. Gohle, R. Holzwarth, *Optics Letters* **29**, 1542 (2004).

9. V. Ataie, *et al.*, *Optical Fiber Communication Conference/National Fiber Optic Engineers Conference 2013* p. OTh3D.2 (2013).

10. J. Sun, E. Timurdogan, A. Yaacobi, E. S. Hosseini, M. R. Watts, *Nature* **493**, 195 (2013).

11. J. C. Hulme, *et al.*, *Optics Express* **23**, 5861 (2015).

12. N. Akhmediev, A. Ankiewicz, *Dissipative Solitons*, Lecture Notes in Physics (Springer Berlin Heidelberg, 2005).

13. T. Herr, *et al.*, *Nature Photonics* **8**, 145 (2013).

14. L. A. Lugiato, R. Lefever, *Phys. Rev. Lett.* **58**, 2209 (1987).

15. M.-G. Suh, Q.-F. Yang, K. Y. Yang, X. Yi, K. J. Vahala, *Science* **354**, 600 (2016).

16. P. Marin-Palomo, *et al.*, *Nature* **546**, 274 (2017).

17. J. D. Jost, *et al.*, *Optica* **2**, 706 (2015).

18. M. H. P. Pfeiffer, *et al.*, *Optica* **3**, 20 (2016).

19. H. Guo, *et al.*, *Nature Physics* **13**, 94 (2017).

20. Materials and methods are available as supplementary materials on *Science* Online.

21. C. Koos, C. Weimann, J. Leuthold, Multiscale distance measurement with frequency combs (2013). U.S. Patent 20150070685.

22. N. Lindenmann, *et al.*, *Optics Express* **20**, 17667 (2012).

23. P.-I. C. Dietrich, *et al.*, *Conference on Lasers and Electro-Optics* p. SM1G.4 (2016).

24. M. Pu, L. Ottaviano, E. Semenova, K. Yvind, *Optica* **3**, 8 (2016).

25. V. Brasch, *et al.*, *Science* **351**, 357 (2016).

26. C. Weimann, *et al.*, *Journal of Physics: Conference Series* **605**, 012030 (2015).

27. J. S. Levy, *et al.*, *Nature Photonics* **4**, 37 (2010).

28. A. Kordts, M. Pfeiffer, H. Guo, V. Brasch, T. J. Kippenberg, *Optics letters* **41**, 452 (2015).

29. D. C. Montgomery, E. A. Peck, G. G. Vining, *Introduction to linear regression analysis* (Wiley, 2012).

30. J. Ronnau, S. Haimov, S. P. Gogineni, *Remote Sensing Reviews* **9**, 27 (1994).

Acknowledgments

Supplementary Materials

Materials and Methods

Figs. S1 to S6

Table S1

References *(26-30)*

Fig. 1. Dissipative Kerr Soliton (DKS) generation in silicon nitride microresonators. (A) SEM-image of a silicon nitride microresonator having a radius of $240\,\mu$m. The checker-board pattern results from the photonic Damascene fabrication process (*18*). **(B)** Visualization of the backward tuning technique. The pump laser wavelength is changed from an effective blue-detuning into an effective red-detuned state thereby increasing the intra-cavity power and giving rise to modulation instability (arrow I). Eventually, the intra-cavity field switches from this chaotic state into a multi-soliton state, when the laser-tuning is stopped. From thereon, the laser wavelength is tuned towards lower wavelengths, decreasing the number of solitons until a single soliton state is reached. The decreasing number of solitons is visible by the decreasing steps of the intra-cavity power (arrow II). **(C)** Spectrum of a DKS optical frequency comb with zoom-in. The spectrum combines large bandwidth and a smooth spectral envelope and features a line spacing of approximately $100\,$GHz.

Fig. 2. Experimental demonstration and performance characterization. (A) Experimental setup. DKS combs are generated by a pair of silicon nitride (Si_3N_4) microresonators, which are pumped by free-running continuous-wave (CW) lasers and erbium-doped fiber amplifiers (EDFA). After suppressing residual pump light by a fiber Bragg gratings (not shown), the combs are amplified by another pair of EDFA. The signal comb (red) is split and one part is routed to the target and back to a balanced measurement photodetector (Meas. PD) by optical fibers, an optical circulator (CIRC) and a collimator (COL), while the other part is directly sent to the balanced reference detector (Ref. PD). Similarly, the LO comb is split in two portions, which are routed to the measurement PD and the reference PD for multi-heterodyne detection. The resulting baseband beat signals are recorded by a 33 GHz real-time sampling oscilloscope. Digital signal processing is performed offline. **(B)** Numerically calculated Fourier transform of a recorded time-domain signal. **(C)** Optical spectra of the signal comb (red) and the local oscillator comb (blue) after amplification. **(D)** Allan deviation of measured distances as a function of averaging time. The increase towards longer averaging times is attributed to drifts and to mechanical vibrations of the fibers that lead to the target (*20*). **(E)** Top: Scan of measured position vs. set position in steps of $50\,\mu$m over the full ambiguity distance (marked by dashed lines). Bottom: Residual deviations ("residuals") between measured and set positions with standard deviations as error bars.

Fig. 3. Reproducibility, benchmarking and ultrafast ranging demonstration. **(A)** Setup for reproducibility and benchmarking experiments: The measurement beam is focused on the surface of a spinning disk having grooves of different depths. **(B)** Measured surface profile of the disk as a function of position (bottom scale) and time (top scale). The plot contains two independent measurements depicted in blue and green. **Inset 1:** Reproducibility demonstration by detailed comparison of the two independent measurements plotted in (B). The measured profiles exhibit good agreement regarding both macroscopic features such as the groove depth as well as microscopic features. **Inset 2:** Benchmarking of the high-speed dual-DKS-comb measurement to the results obtained from an industrial optical coordinate-measuring machine (CMM). **(C)** Setup of ultrafast ranging experiment. **(D)** Measured profile of the projectile obtained from single-shot in-flight dual-DKS-comb measurement (red), along with a swept-source OCT profile scan that was recorded on the static projectile after recovery from the backstop. The deviations towards the back end of the projectile are attributed to strong corrugations in this area, see (E). **(E)** Image of the projectile after recovery from the backstop.

Fig. 4. Artist's view of a dual-comb chip-scale LIDAR engine. The system consists of a dual frequency comb source (A), a photonic integrated circuit (PIC) for transmission and detection of the LIDAR signal (B), as well as data acquisition and signal processing electronics (C). The system is realized as a photonic multi-chip assembly that combines the distinct advantages of different photonic integration platforms. The insets show various technologies that could be used to realize the envisioned LIDAR engine. **Inset 1:** Si_3N_4 microresonator for comb generation (*18, 25*). **Inset 2:** Photonic wire bonds for chip-chip connections (*22*). **Inset 3:** Facet-attached micro-lens for collimation of the emitted free-space beam (*23*).
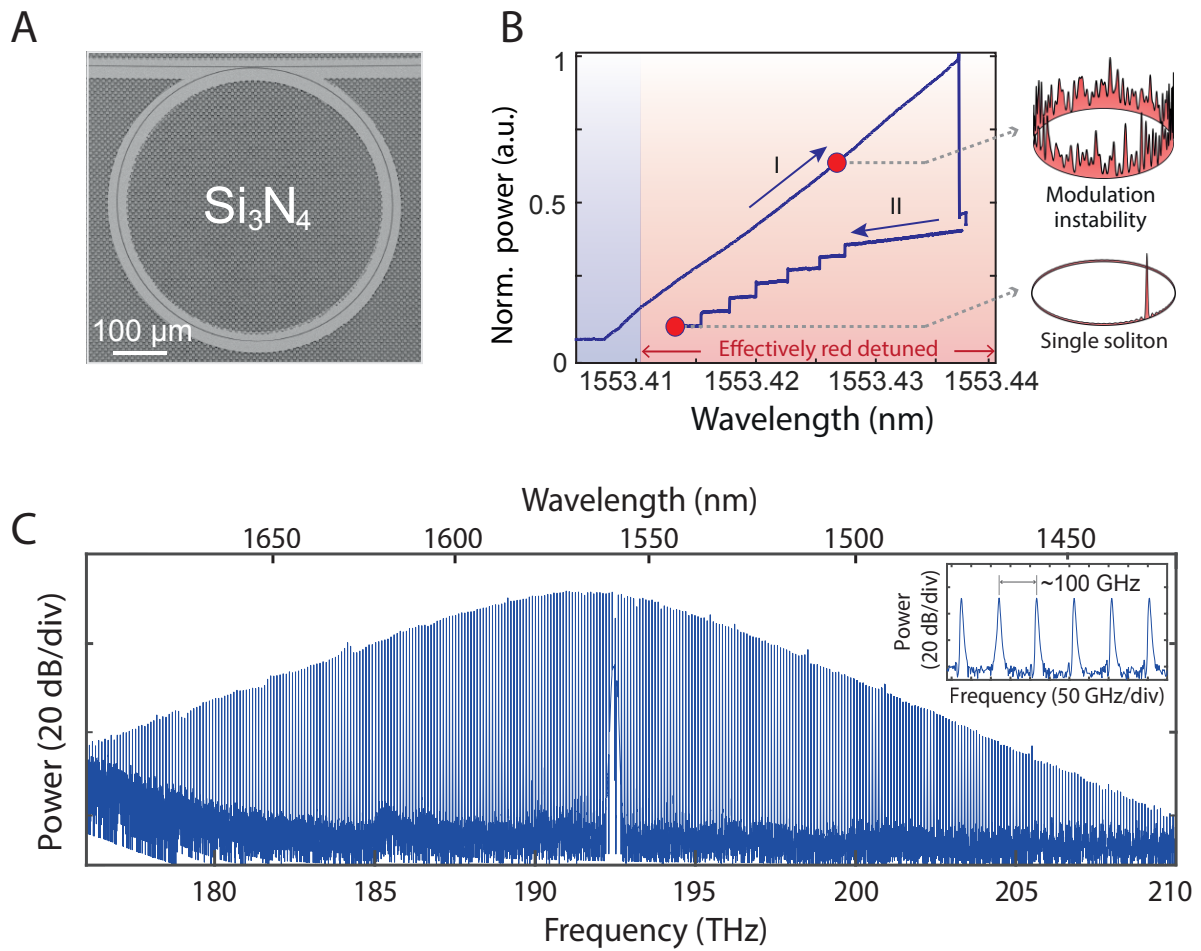
Figure 1: **Dissipative Kerr Soliton (DKS) generation in silicon nitride microresonators.**
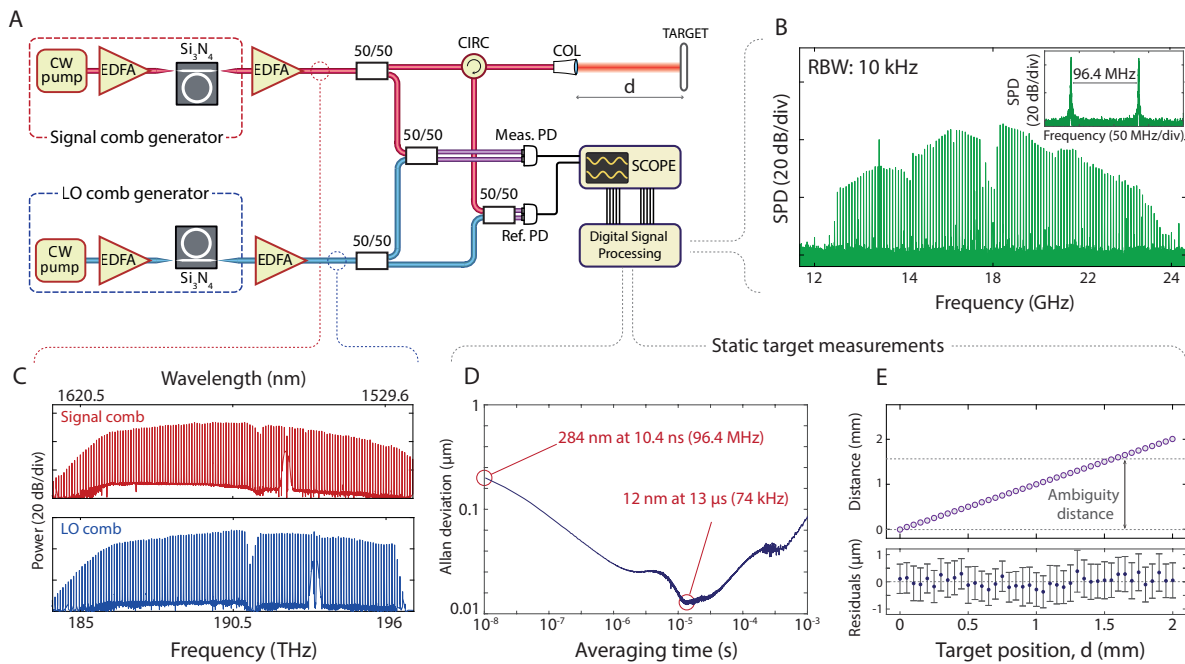
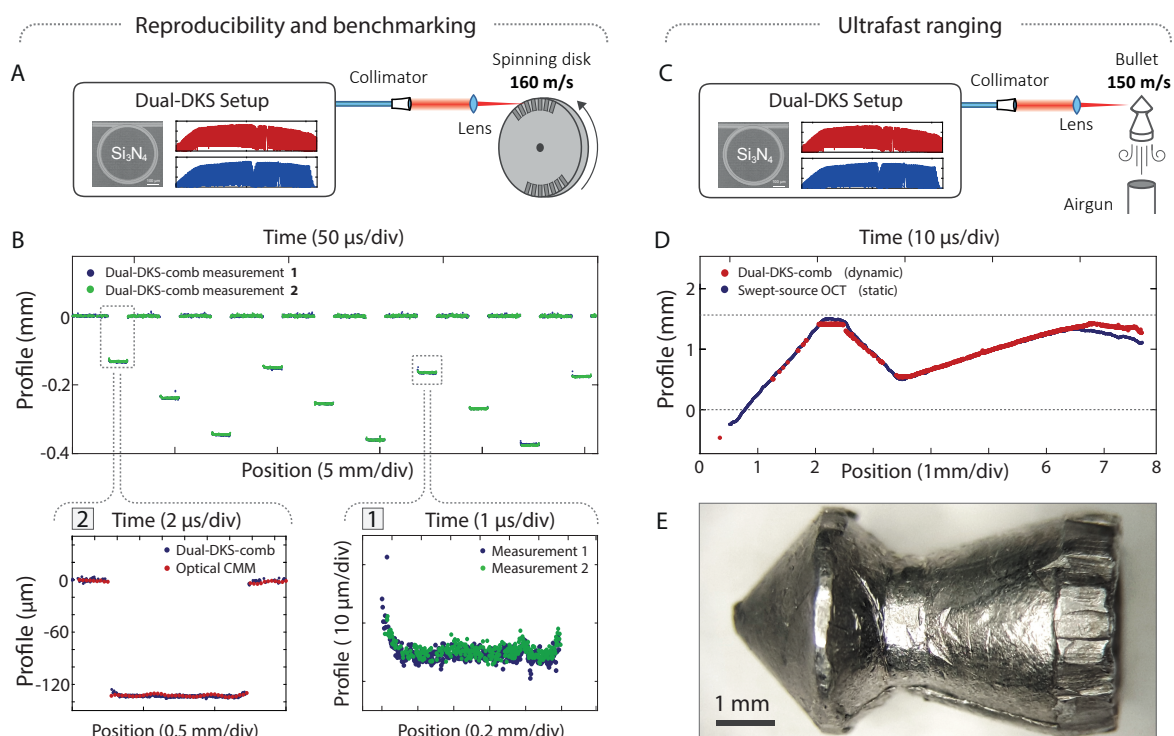Figure 2: **Experimental demonstration and performance characterization.**

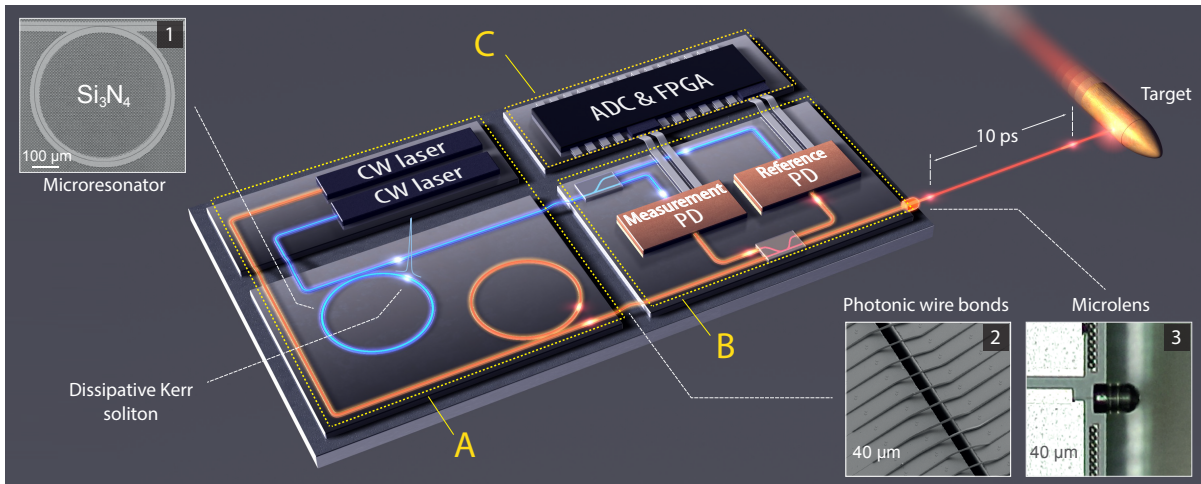Figure 3: **Reproducibility, benchmarking and ultrafast ranging demonstration.**

Figure 4: **Artist's view of a dual-comb chip-scale LIDAR engine.**